Liquefaction and Related Ground Failure from July 2019 Ridgecrest Earthquake Sequence

Paolo Zimmaro[*1], Chukwuebuka C. Nweke[1], Janis L. Hernandez[2], Kenneth S. Hudson[1], Martin B. Hudson[3], Sean K. Ahdi[4,5], Matthew L. Boggs[6], Craig A. Davis[7], Christine A. Goulet[8], Scott J. Brandenberg[1], Kenneth W. Hudnut[1,9], and Jonathan P. Stewart[1]

ABSTRACT

The 2019 Ridgecrest earthquake sequence produced a 4 July M 6.5 foreshock and a 5 July M 7.1 mainshock, along with 23 events with magnitudes greater than 4.5 in the 24 hr period following the mainshock. The epicenters of the two principal events were located in the Indian Wells Valley, northwest of Searles Valley near the towns of Ridgecrest, Trona, and Argus. We describe observed liquefaction manifestations including sand boils, fissures, and lateral spreading features, as well as proximate non-ground failure zones that resulted from the sequence. Expanding upon results initially presented in a report of the Geotechnical Extreme Events Reconnaissance Association, we synthesize results of field mapping, aerial imagery, and inferences of ground deformations from Synthetic Aperture Radar-based damage proxy maps (DPMs). We document incidents of liquefaction, settlement, and lateral spreading in the Naval Air Weapons Station China Lake US military base and compare locations of these observations to pre- and postevent mapping of liquefaction hazards. We describe liquefaction and ground-failure features in Trona and Argus, which produced lateral deformations and impacts on several single-story masonry and wood frame buildings. Detailed maps showing zones with and without ground failure are provided for these towns, along with mapped ground deformations along transects. Finally, we describe incidents of massive liquefaction with related ground failures and proximate areas of similar geologic origin without ground failure in the Searles Lakebed. Observations in this region are consistent with surface change predicted by the DPM. In the same region, geospatial liquefaction hazard maps are effective at identifying broad percentages of land with liquefaction-related damage. We anticipate that data presented in this article will be useful for future liquefaction susceptibility, triggering, and consequence studies being undertaken as part of the Next Generation Liquefaction project.

KEY POINTS

- We show occurrences of liquefaction manifestation, or lack, thereof following the 2019 Ridgecrest earthquakes.
- Radar-based damage proxy maps were able to identify areas where liquefaction-related surface change occurred.
- Geospatial liquefaction hazard maps can identify broad percentages of land with liquefaction-related damage.

Supplemental Material

INTRODUCTION

The Ridgecrest earthquake sequence, including the 4 July **M** 6.5 foreshock and the 5 July 2019 **M** 7.1 mainshock, occurred on faults formerly considered as part of the greater Little Lake fault zone, now differentiated after the recent earthquakes and referred to as the Salt Wells Valley fault zone for the **M** 6.5 event and the Paxton Ranch fault zone for the **M** 7.1 event (T. Dawson *et al.*, unpublished manuscript, 2020, see Data and Resources). The moment magnitudes used in this article are computed from seismic moments provided in the Global Centroid-Moment-Tensor (GCMT) project database

1. Department of Civil and Environmental Engineering, University of California, Los Angeles, California, U.S.A.; 2. Department of Conservation, California Geological Survey, Los Angeles, California, U.S.A.; 3. Turner Engineering Group, Turner Construction Company, Los Angeles, California, U.S.A.; 4. Exponent, Inc., Los Angeles, California, U.S.A.; 5. Department of Earth, Planetary, and Space Sciences, University of California, Los Angeles, California, U.S.A.; 6. Naval Air Warfare Center—Weapons Division, US Navy, China Lake, California, U.S.A.; 7. City of Los Angeles Department of Water and Power (Retired), Los Angeles, California, U.S.A.; 8. Southern California Earthquake Center, University of Southern California, Los Angeles, California, U.S.A.; 9. U.S. Geological Survey, Pasadena, California, U.S.A.

*Corresponding author: pzimmaro@ucla.edu

Cite this article as Zimmaro, P., C. C. Nweke, J. L. Hernandez, K. S. Hudson, M. B. Hudson, S. K. Ahdi, M. L. Boggs, C. A. Davis, C. A. Goulet, S. J. Brandenberg, *et al.* (2020). Liquefaction and Related Ground Failure from July 2019 Ridgecrest Earthquake Sequence, *Bull. Seismol. Soc. Am.* **110**, 1549–1566, doi: 10.1785/0120200025

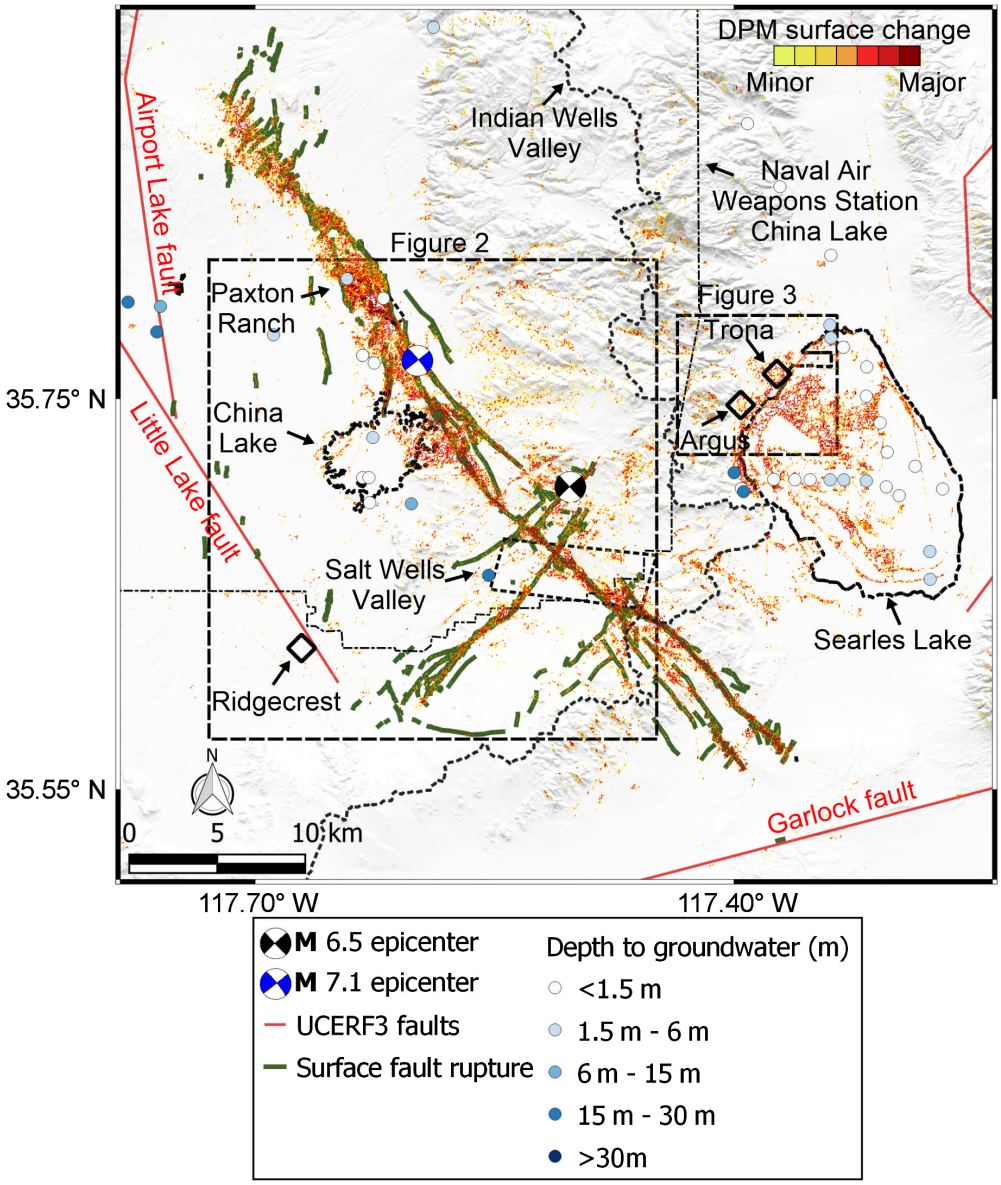

Figure 1. Overview of the Ridgecrest 2019 earthquake sequence epicentral area showing mapped surface fault rupture features following the **M** 6.5 and **M** 7.1 events (from Ponti *et al.*, 2020) and locations of surface change, as provided on a damage proxy map (DPM) produced following the **M** 7.1 event. Fault traces are from the Uniform California Earthquake Rupture Forecast, version 3 (UCERF3) model (Field *et al.*, 2014). Observation well data were obtained from California Department of Water Resources (DWR). Moment tensors were obtained from the Global Centroid-Moment-Tensor (GCMT) project (Ekström *et al.*, 2012) (see Data and Resources). Outlines of detailed maps are in Figures 2 and 3 shown. The color version of this figure is available only in the electronic edition.

(Ekström *et al.*, 2012). The two fault zones are part of the eastern California shear zone (ECSZ), a northward extension of the right-lateral southern San Andreas fault tectonic regime that continues northward through the Owens Valley toward Walker Lane. This zone is bordered to the east by the extensional Basin and Range province. As shown in Figure 1, developed areas locally affected by the sequence include the Naval Air Weapons Station (NAWS) China Lake, the City of Ridgecrest, and the two nearby towns of Trona and Argus in the adjacent Searles Valley. An extensively investigated feature of these events was substantial surface rupture along the causative faults, which is presented by Ponti *et al.* (2020) and T. Dawson *et al.* (unpublished manuscript, 2020, see Data and Resources). In this article, we describe significant liquefaction-related effects, as well as proximate areas without ground failure, in Searles Valley and Indian Wells Valley.

Following the 4 July 2019 **M** 6.5 event, multiagency reconnaissance teams deployed to the epicentral area to collect perishable information such as ground-failure features and related effects on buildings and infrastructure. The information presented in this article represents composite findings from the following teams deployed in the field at various points in time with different focuses and objectives, and utilizing a variety of different reconnaissance tools:

- Geotechnical Extreme Events Reconnaissance (GEER) team (Stewart *et al.*, 2019; Brandenberg, Stewart, *et al.*, 2020): on-ground mapping and aerial imagery by means of small Uninhabited Aerial Systems (sUAS) focusing on earthquake effects in Trona, Argus, and some portions of the surface fault rupture features (July and August 2019);
- U.S. Geological Survey (USGS), California Geological Survey (CGS), and U.S. Navy team: on-ground mapping, helicopter overflights, as well as aerial and ground surface photography focusing on the NAWS China Lake in Indian Wells Valley (July–September 2019); and
- National Aeronautics and Space Administration (NASA)-supported team: on-ground mapping of ground-failure-related damage within the Searles Lake area (November 2019; Zimmaro and Hudson, 2019).

The main objectives of this article are to: (1) document occurrences of liquefaction and adjacent areas of nonground failure, so as to facilitate the utilization of this data in liquefaction databases (e.g., Schmitt *et al.*, 2017; Brandenberg, Zimmaro, *et al.*, 2020); (2) demonstrate the effective utilization of multiple information sources to study liquefaction effects across a broad region with variable access; and (3) use field observations of ground failure to validate spatial data tools including near real-time liquefaction hazard maps produced by USGS and Synthetic Aperture Radar (SAR)-based damage proxy maps (DPMs) produced by the Advanced Rapid Imaging and Analysis (ARIA) team at the California Institute of Technology (Caltech) and the NASA—Jet Propulsion Laboratory (JPL). All data collected by the GEER- (Brandenberg *et al.*, 2019; Brandenberg, Stewart, *et al.*, 2020) and NASA-supported (Zimmaro and Hudson, 2019) teams presented and discussed in this article are available on DesignSafe (Rathje, Secara, *et al.*, 2017). Additional data from the USGS-CGS-US Navy reconnaissance team, such as aerial and ground-based photos of liquefaction and other water-related ground-failure features, which were observed after the **M** 6.5 (but before the **M** 7.1) as well as after the **M** 7.1 event, are reported in supplemental material available to this article (Table S1; Figs. S1–S17). A few of the ground-failure features documented in this article were also briefly noted by Jibson (2020).

NEAR REAL-TIME DAMAGE AND LIQUEFACTION MAPS

DPMs

Following major natural and/or anthropogenic events, the ARIA team at Caltech and NASA JPL produces near real-time maps to identify the extent of potentially damaged areas. These DPMs are produced utilizing SAR images. Such techniques are based on differences in phase of radio waves returning to a moving platform. In the case of the DPMs, these platforms are satellites. DPMs are produced by comparing interferometric SAR coherence maps from before and after an extreme event (e.g., Fielding *et al.*, 2005; Yun *et al.*, 2011). Such maps are typically produced following major earthquakes, hurricanes, floods, and wildfires. A known issue with SAR-based data is that damage detection is challenging in areas with potential sources of noise, including vegetation coverage, steep topography, and areas where the landscape is modified over a short period of time (e.g., due to human activities). The study region in Figure 1 contains sparse plant cover. Furthermore, anthropogenic activities only occur in a small portion of this region, as it mainly consists of undeveloped land that is publicly inaccessible. As a result, it provides a nearly ideal setting for validating DPM predictions.

DPMs and similar SAR-based products have previously been compared against observations following recent events, including the 2011 **M** 9.1 Tohoku earthquake (Ishitsuka *et al.*, 2012), the 2015 **M** 7.8 Gorkha earthquake (Yun *et al.*, 2015), the 2016 central Italy earthquake sequence (Franke *et al.*, 2018; Sextos *et al.*, 2018), and the 2018 **M** 6.6 Hokkaido earthquake (Jung and Yun, 2020). These comparisons show good general agreement between areas with building and/or ground-failure damage and DPMs. However, additional high-quality observations are needed to develop formal quantitative metrics to analyze the reliability of such maps. As a result, the ground-truth data presented in this article constitute a valuable resource to validate DPMs and similar remote-sensing products against liquefaction and related ground failure.

A public DPM was released following the 12 July 2019 Ridgecrest earthquake sequence (see Data and Resources). Figure 1 shows the DPM, observed surface rupture features, and outlines of more detailed maps showing liquefaction features presented in this article. The DPM in Figure 1 covers an area of 300 × 250 km. Each pixel in the map is 30 × 30 m. This level of resolution can be used to detect regions with high damage. However, it may be too coarse to identify small damage features such as pavement cracks, individual sand boils, or damage to individual buildings. The map was created using SAR data available from the Copernicus Sentinel-1 satellites, operated by the European Space Agency.

The DPM in Figure 1 is based on pre- and postevent SAR images taken before the 4 July 2019 **M** 6.5 event and after the 10 July 2019 **M** 7.1 event. During the period between the two image acquisitions, 30 earthquakes with magnitude greater than 4.5 were recorded in the area (USGS, 2020). As a result, damage proxies result from the cumulative effects of multiple events. This map shows colored pixels only where coherence loss values are above the noise threshold (defined by the map developers). These colored pixels represent zones where the map identifies significant surface change (nonzero damage proxies). Pixels with an associated coherence loss lower than the noise threshold are not shown in the map. The map captures well the observed fault surface rupture features from both the **M** 6.5 and **M** 7.1 events. It also shows extensive surface change within the Searles Lake area and more distributed surface changes in the Paxton Ranch and Salt Wells Valley areas. In the remainder of the article, we compare observed liquefaction surface manifestations to spatial data tools, including DPM predictions, in greater detail.

USGS liquefaction hazard maps

As part of the Earthquake Hazards Program, the USGS developed a ground-failure earthquake product to augment the Prompt Assessment of Global Earthquakes for Response system (see Data and Resources). Following major earthquakes worldwide, this product provides near real-time maps of earthquake-induced landslide and liquefaction probabilities. Both the liquefaction and landslide maps are derived from models that utilize ground-shaking intensity as an input, which allows the maps to be rapidly generated, but which does not take into account information from remotely sensed images, as the DPMs do.

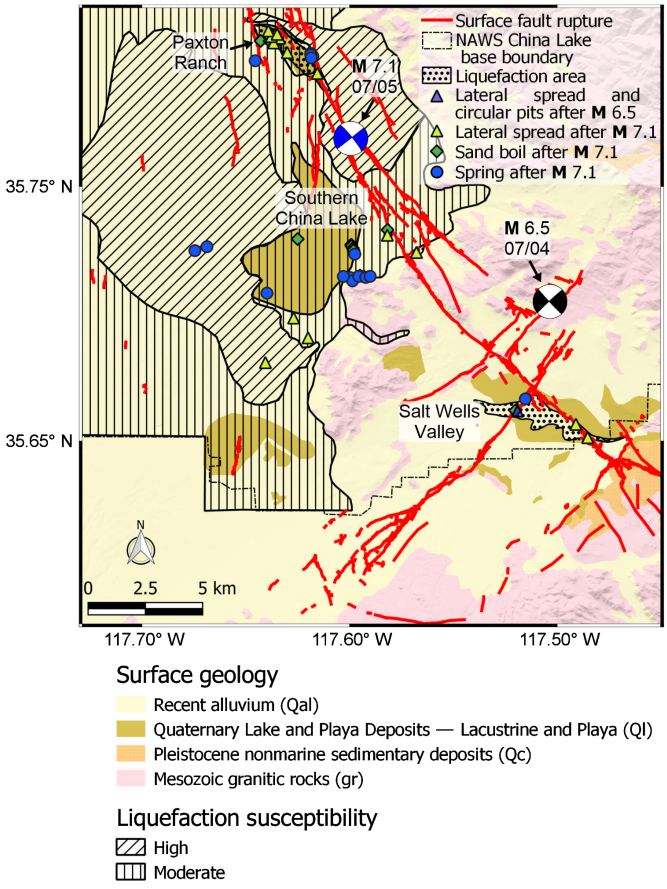

Figure 2. Surface geologic map of eastern portion of Indian Wells Valley (from Jennings *et al.*, 1962) showing locations of mapped liquefaction features. Liquefaction susceptibility zones modified from mapping by Banks (1982). The color version of this figure is available only in the electronic edition.

Geospatial liquefaction models are used to generate the liquefaction hazard maps, which are conditioned on ground motion parameters and globally available inputs. The two models currently used are:

- Preferred model: Zhu *et al.* (2017) with additional modifications by Baise and Rashidian (2017)
- Alternate model: Zhu *et al.* (2015)

Ground-motion inputs are taken from ShakeMaps (Wald *et al.*, 2005; Worden *et al.*, 2020), which, in turn, are derived from instrumental recordings, ground-motion models, and site conditions estimated from topographic slope (Wald and Allen, 2007). Additional inputs related to liquefaction vulnerability include mean annual precipitation (from Hijmans *et al.*, 2005), distance from the coast (from NASA Ocean Color Group, see Data and Resources), distance from rivers (from the HydroSHEDS database, see Data and Resources), and water table depth (from Fan *et al.*, 2013).

The USGS liquefaction hazard maps estimate liquefaction areal coverage. The probability values in these maps are predicted percentages of land area affected by liquefaction, within 500 × 500 m cells.

The USGS published liquefaction hazard maps following each of the **M** 6.5 and **M** 7.1 events. Because most of the liquefaction features were observed following the **M** 7.1 mainshock, in the remainder of the article, we compare field observations to the second USGS liquefaction hazard map (version 4, released on 8 July 2020, see Data and Resources).

REGIONAL GEOLOGIC SETTING, GEOLOGIC MATERIALS, AND GEOHYDROLOGY

Indian Wells Valley and Searles Valley are located in the southwestern corner of the Basin and Range geomorphic province near its interface with the Mojave Desert geomorphic province. The northern portion of the Basin and Range province is called the Great Basin region, which is approximately bounded by the Garlock fault on the south and the Sierra Nevada Mountains on the west, and extends to the Colorado plateau to the east and the Columbia plateau to the north. The province is characterized by interior drainage with lakes and playas and horst-and-graben geologic structure (subparallel, fault-bounded ranges separated by down-dropped basins) that include valleys such as Death Valley, Owens Valley, Honey Lake Basin, and associated mountain ranges. The Mojave Desert geomorphic province is bound by the Garlock fault on the north and the San Andreas fault on the southwest and extends east to the Colorado plateau. The Mojave Desert province is characterized by a broad interior of isolated mountain ranges separated by desert plains.

Both Indian Wells Valley and Searles Valley are alluvial basins characterized by alluvial fan deposits on the flanks of the surrounding mountains with lacustrine deposits in the interior of the basins. The alluvial deposits are derived from the surrounding mountains, which are primarily Paleozoic to late Mesozoic granitic bedrock (Kunkel and Chase, 1969) and volcanic deposits (Schweig, 1984).

Indian Wells Valley contains a dry playa called China Lake, which is located at an approximate elevation of 650 m above mean sea level (AMSL) (North American Vertical Datum of 1988 [NAVD 88]). Searles Valley also contains a playa called Searles Lake at an approximate elevation of 490 m AMSL (NAVD 88).

As shown in Figure 2, there are three distinct geologic units within the Indian Wells Valley: alluvium (including some windblown dune deposits), lacustrine deposits, and playa deposits, as described by Berenbrock and Schroeder (1994) and Bullard *et al.* (2019). The alluvium consists of moderate- to well-sorted gravel, sand, silt, and clay of Pleistocene and Holocene ages, and continues to be actively deposited. The fines content increases, and the thickness of alluvial deposits decreases toward the central portion of China Lake. Lacustrine deposits contain silt and silty clay of Pleistocene age, and overlies the alluvial deposits in the center of the basin (Kunkel and

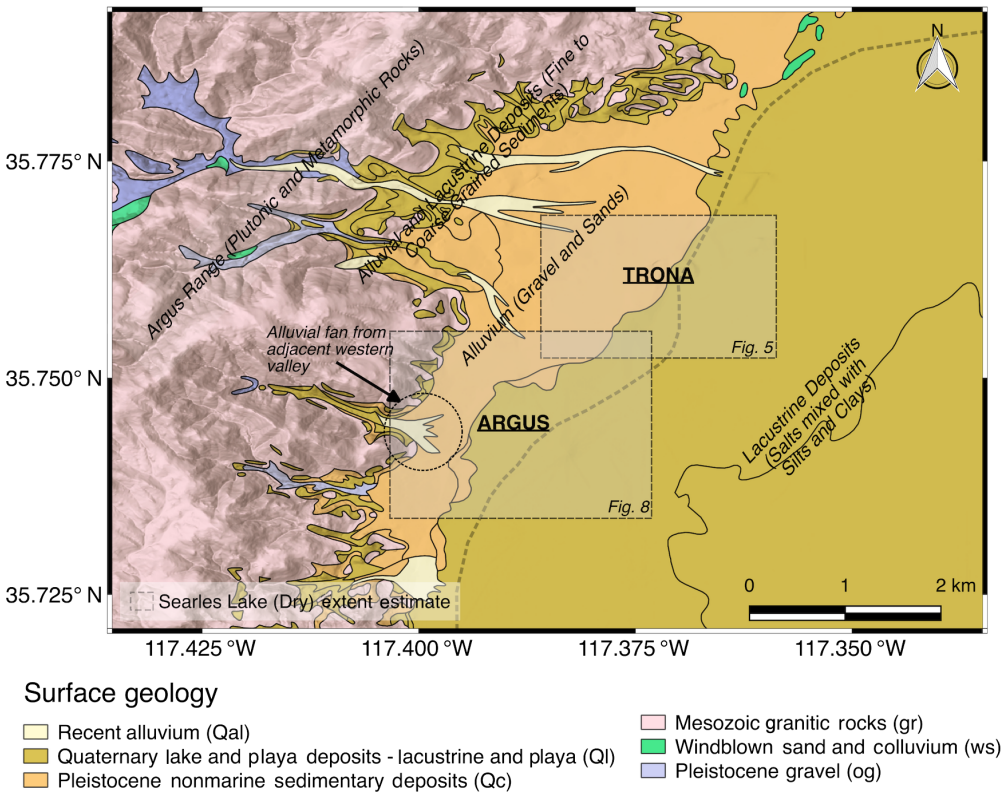

Figure 3. Map of the northwestern portion of Searles Valley showing the general geologic material underlying the towns of Trona and Argus. The estimated extent of the dry Searles Lake is also depicted. The color version of this figure is available only in the electronic edition.

(Fig. 1). Within the Indian Wells Valley groundwater basin, the depth to groundwater varies from the ground surface in the center of the valley near Paxton Ranch to greater than 100 m below ground surface (bgs) on the margins of the valley (California DWR, 2020). Within the Salt Wells Valley groundwater basin, there is groundwater at the ground surface in the center of the basin to greater than 15 m bgs along the margins (California DWR, 2020). The Searles Valley groundwater basin has surface water present in the central–western portion of the Searles Lake playa associated with mining activity from the Searles Valley Minerals, Inc. Groundwater throughout the playa ranges from less than 1 to approximately 2 m bgs (California DWR, 2020). The groundwater in this basin is a brine with pH values between 9.2 and 9.5 (Smith, 1979).

Chase, 1969). Playa deposits consisting of silt and clay with occasional sand lenses that overlie the lacustrine deposits are Holocene in age and are being actively deposited. The aeolian sand dune deposits are Holocene in age (Warner, 1975; Lancaster *et al.*, 2019).

As shown in Figure 3 (vicinity of Trona and Argus), Searles Valley has a similar stratigraphy to Indian Wells Valley with Pleistocene and Holocene alluvium, consisting of fine-to-coarse sand with little gravel and fines, Holocene playa silt and clay, and Holocene aeolian dune sand. However, the lacustrine deposits differ in that they contain thick evaporite deposits interbedded with lacustrine silts and clays. The evaporites consist primarily of halite, thermonatrite, thenardite, and ulexite with gypsum, locally common in some units (Smith, 2009).

The two valleys include two hydrographically closed groundwater basins: Indian Wells Valley and Searles Valley Groundwater Basins of the South Lahontan Hydrologic Region (California Department of Water Resources [DWR], 2003). The Salt Wells Valley groundwater basin is located between the two. During the Pleistocene, the region was much wetter, and these currently isolated groundwater basins were connected by the Owens River (McGraw *et al.*, 2016).

Based on data from observation wells collected in the period 1959–2019, we show the depth to ground water in the study area

SITES AT NAWS CHINA LAKE

The NAWS China Lake base is located within the Basin and Range geomorphic province of California, within the ECSZ. Developed areas within the NAWS China Lake are primarily within the Indian Wells Valley. Our observations of liquefaction-related ground-failure features in the NAWS were focused primarily within lacustrine and playa deposits.

Reconnaissance methods

Methods of recording liquefaction features included post-earthquake helicopter overflights and field geologic mapping. High-quality single-lens reflex imagery was used to record observations with Global Positioning System (GPS)-enabled locations as well as digital photos collected using ArcCollector software on iPad tablets. Both types of imagery were collected in overflight reconnaissance and during field verification. Limits of liquefaction were generally noted during overflight observations. The team performed a subsequent ground deployment, targeting surface-fault rupture areas. During this field deployment, liquefaction features were visited on the ground, when they were near to surface-rupture locations. Because of time constraints with helicopter overflights, available NAWS escorts, and USGS-CGS field teams, our observations focused on primary surface rupture. Overflight

reconnaissance was performed at an elevation of about 150 m above the ground surface or less.

The first helicopter overflight and collection of aerial photography were completed on the afternoon of 5 July 2019, after the **M** 6.5 foreshock, and prior to the **M** 7.1 mainshock. The next day, helicopter reconnaissance was again performed following the predominantly northwest-oriented surface rupture associated with the 5 July 2019 **M** 7.1 mainshock. Several other overflights were performed on subsequent days. CGS and USGS geologists paired up daily as earthquake response teams, in which the primary focus was to document and measure surface rupture and to obtain geolocated photographs of any liquefaction-related or ground-failure features. Track logs of these helicopter flights are shown in Figures S18 and S19.

Findings

Review of the distribution of liquefaction-related features was performed by identifying liquefaction features from CGS staff photographs and entering GPS coordinates of each photo into an ESRI ArcGIS geodatabase and map. The GPS coordinates of photos taken during overflights refer to the location of the helicopter. However, we tried, when possible, to identify persistent features on the ground and report the actual location of the observation, rather than the location of the helicopter. As a result, locations of observations made during overflights refer as best as possible to their actual location on the ground. Data were subdivided into separate categories of liquefaction surface manifestations and other ground-failure features such as sand boils, lateral spreading, and seepage or springs. Areas with widespread liquefaction features were then delineated into separate polygons, as shown in Figure 2.

For the NAWS base observations, Table S1 presents locations of liquefaction features observed during postearthquake reconnaissance, grouped into areas A–C (North Dry Lakebed Area—Paxton Ranch, central Area—southeast end of China Lake, and southern Area—Salt Wells Valley, respectively). Figures S1–S17 show photos of representative liquefaction effects at selected locations discussed in this section and listed in Table S1.

As shown in Figure 2, areas of liquefaction-related ground failures from the Ridgecrest earthquake sequence are found within three primary areas on the NAWS base: Paxton Ranch, the southern end of China Lake Playa, and Salt Wells Valley. Site conditions in which liquefaction features exist included saturated or very shallow groundwater levels, loose, fine-grained playa and lacustrine sediments, and areas where natural springs occur at bedrock–alluvium contacts. In addition, near the southern edge of the China Lake playa, leakage from the sewage ponds, and corresponding drainage channels from Lark Seep to the playa are a contributing factor. Seasonal rains collect in both the China Lake and Salt Wells Valley areas, promoting shallow groundwater conditions.

Liquefaction features appeared to coincide with surface-fault rupture locations in the Paxton Ranch area. Lateral spreads were prominent throughout the central portion of the small playa in this area and concentrated just inside the outer edges of the playa (Fig. 2 and Fig. S1). Ground failures that occurred in the Paxton Ranch area did not appear to impact infrastructure, as these features appeared to be fairly constrained to the small, unnamed northern playa surface.

In southern China Lake, springs or seeps were located within the playa deposits, approximately 35–50 m from the bedrock–alluvium contact (35.714920°, −117.592197°). Based on pre- and postevent satellite imagery, we determined that these features were triggered by the 2019 earthquake sequence. Large sand boils with central openings 2–4 m in diameter were located 125–160 m west of the main **M** 7.1 surface rupture (35.733098°, −117.582061°), as shown in Figure 2 and Figure S8. Ground failures were noted in the China Lake area at a sewer treatment pump house, located within the eastern portion of China Lake playa, about 1.7 km west of the main **M** 7.1 rupture. Damage to this structure included excavation backfill settlement (ring fractures) and external pipe connection dislocations. Foundation settlement was not observed, although shallow groundwater pumping extended outside the building, and some external utility poles were tilted. Lateral spread features were observed along the southern end of China Lake playa near a shallow detention basin (35.723812°, −117.567984°), about 70 m away from the bedrock–alluvium contact (Fig. S10). Other buildings located along the southern edge of the China Lake playa (35.711727°, −117.601528°) exhibited foundation settlement, displaced or broken water lines, and tilted utility poles.

In the Salt Wells Valley area, lateral spreads were common near channel margins and along edges of Salt Wells Valley creek in which sediments were moist to wet. Observations of liquefaction features within Salt Wells Valley did not appear to impact infrastructure at the base, and no incidents were reported to us during our reconnaissance. Some ground-failure features (lateral spreads and three circular pits) were observed in the Salt Wells Valley area following the **M** 6.5 event, but prior to the **M** 7.1 mainshock (Fig. 2 and Fig. S14). The lateral spreads were not on the surface rupture, but the three circular pits were immediately on top of the surface rupture (Fig. S14). We think, they may have formed by water flowing into open cracks, as with piping, and may not necessarily be indicative of soil liquefaction. These circular pits did not have ejecta rims. No ground-based investigation was possible until after the **M** 7.1 event, so we only have the photographic evidence from prior to the **M** 7.1 mainshock.

Comparison to pre-event susceptibility map and postevent liquefaction hazard map

In this section, we compare liquefaction observations with a pre-event liquefaction susceptibility map and the postevent USGS liquefaction hazard map. In this area, liquefaction

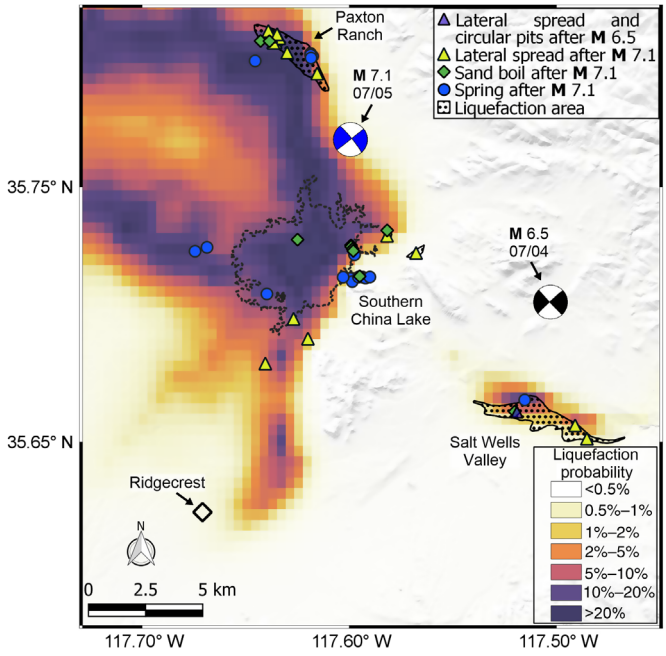

Figure 4. Map of the Indian Wells Valley, observed liquefaction features, and USGS near real-time liquefaction hazard map. The color version of this figure is available only in the electronic edition.

surface manifestations are often coincident with (or located nearby) surface-fault rupture features, the two of which cannot be distinguished by the DPM. As a result, comparisons between observed liquefaction manifestations and the DPM are not possible in this region.

Previous studies for liquefaction potential were performed by Banks (1982), by investigating sediments within Indian Wells Valley to evaluate the possibility of seismically induced liquefaction of sediments beneath important structures at the NAWS. The Banks (1982) study produced a susceptibility matrix that included age of deposit, soil type, and depth to groundwater. The results from that study concluded that much of the study area has a strong likelihood of liquefaction, if earthquake ground motions from a set of five sources (Sierra Nevada, Little Lake, Airport Lake, Argus, Garlock, and background seismicity) with a 100 yr event return period were to occur. As part of the study, a map was produced showing areas with near-surface sediments having high-, moderate-, and nonsusceptible conditions. The Salt Wells Valley was not included in the study by Banks (1982). Portions of the Banks (1982) map that overlapped with our study area were digitized and are included in Figure 2. We find that the map successfully identified locations of liquefaction at Paxton Ranch and Southern China Lake, but that it did not predict the liquefaction effects at the margin of China Lake, and predicted large zones of liquefaction susceptibility where no effects were observed during our field visits (i.e., false positives). This mismatch was likely influenced by the map having been derived from older groundwater depths and precipitation catalogs and having limited information on soil-type, both of which are factors that control liquefaction susceptibility.

Figure 4 shows the near real-time liquefaction probability map produced by USGS following the **M** 7.1 mainshock. The map predicts high probability of liquefaction within China Lake, the Salt Wells Valley, and in the Paxton Ranch area. The spatial distribution of liquefaction surface manifestation in these regions seems to be consistent with the prediction of the liquefaction hazard map. In these areas, the predicted probability of liquefaction ranges between 5% and 20%. In the western portion of Figure 4 and Figure S19, west of China Lake, the predicted probability map does not appear to be consistent with our on-ground and overflight observations.

TRONA AND ARGUS

Trona and Argus are situated near the northwestern margin of Searles Lake (Fig. 3). Geologic features include lacustrine deposits along the margin of Searles Lake, alluvial deposits upslope from the lacustrine deposits, and alluvial fans near the base of the hills to the northwest. Liquefaction features were apparent throughout this region.

Reconnaissance methods

The GEER team visited Trona and Argus on 5–7 July 2019 and documented evidence of liquefaction using geotagged digital photos and ground-based mapping techniques using tape measures and GPS track logs. A phase II GEER team subsequently visited sites of interest in Trona and Argus the following week to gather sUAS images that were processed using structure-from-motion techniques to obtain point clouds and digital elevation models. Data from these studies are publicly available and documented by Brandenberg, Stewart, *et al.* (2020). The GEER effort did not focus on Searles Lake due to access restrictions. However, a follow-up visit by a subset of the team in November 2019 with cooperation from Searles Valley Minerals Inc. expanded the locations of observed liquefaction effects (Zimmaro and Hudson, 2019). This reconnaissance effort utilized geotagged photos, GPS track logs, and ground measurements.

Findings

Figure 5 shows locations of observed liquefaction features (sand boils and cracks in hardscape and paving) in Trona and a portion of Searles Lake. Sand boils were encountered along the southern edge of Trona near the northern margin of Searles Lake (e.g., Fig. 6a). Sand boils frequently occurred at discontinuities on the ground surface such as pavement edges, utility fixtures, pre-existing cracks (prior to earthquake sequence), and developed cracks (created as a result of the earthquake sequence). Examples of these various sand boil features are available in the accompanying supplements as well as Brandenberg *et al.* (2019) and Brandenberg, Stewart, *et al.* (2020).

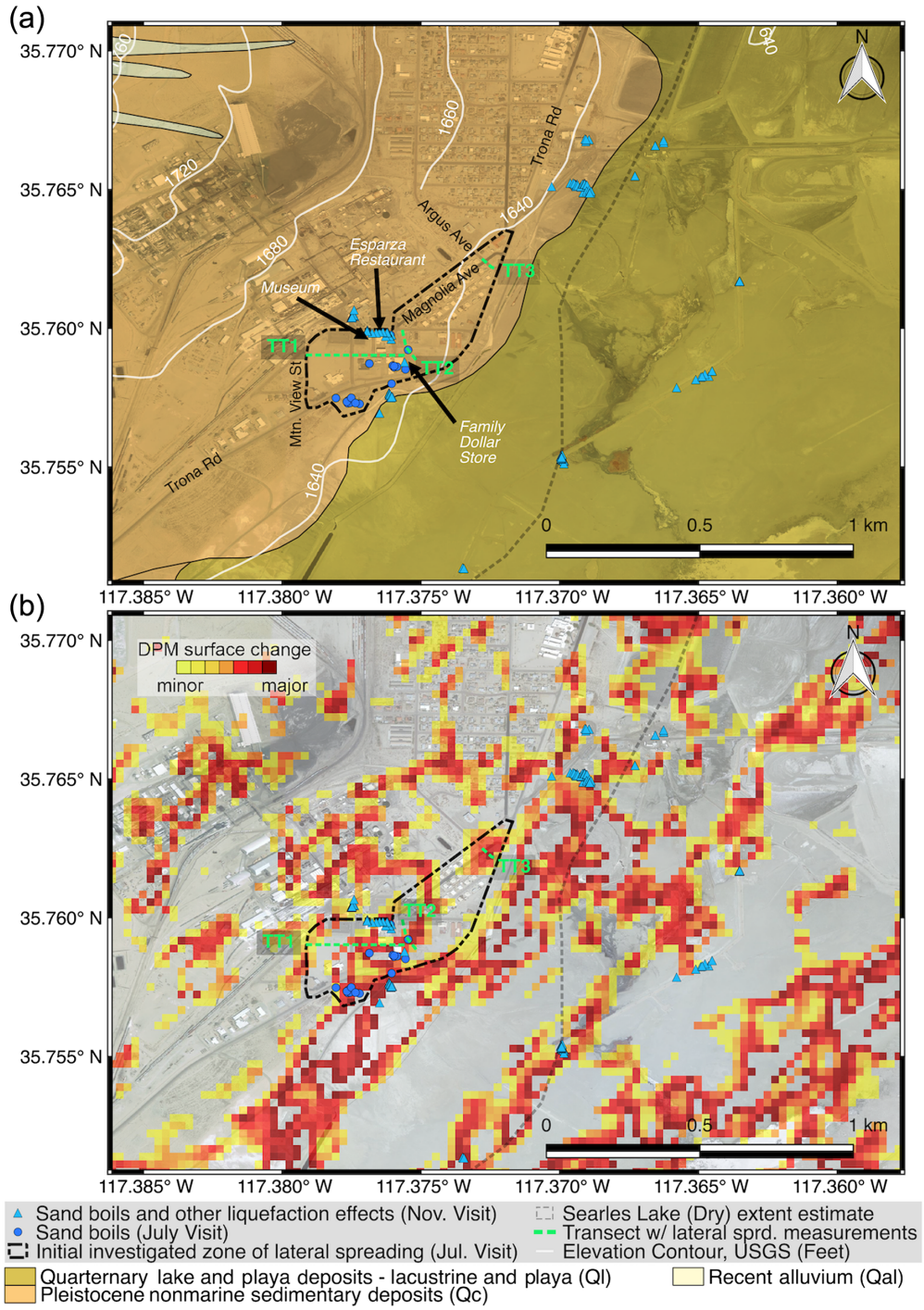

Figure 5. Map of Trona showing locations of observed liquefaction effects and lateral spreading measurement transects overlayed on (a) surface geology map and (b) DPM. Geologic units are labeled following descriptions from Smith (2009). Areas without indications of ground failure within investigated zone were inspected and hence are confirmed no ground-failure zones. The color version of this figure is available only in the electronic edition.

Ground cracks caused by extensional strain due to lateral spreading were apparent near the sand boils and throughout the investigated region (Fig. 6b,c,g). The orientation of the extensional cracks was variable. Many cracks trended toward the northeast, parallel to the lake perimeter, but other cracks were at different angles. We interpret this to indicate that the lateral spreading was predominantly toward the lakebed, but lateral movement occurred in other directions as well, possibly due to the influence of structures on ground displacements or due to ground oscillation (Fig. 6g). In addition to the extensional ground cracks, compressional features were also observed in various regions (Fig. 6d–f,h), as evidenced by buckled concrete curbs and regions where the asphalt pavement cracked and rode up over adjacent pavement.

Field mapping to record locations of cracks and approximate crack widths were performed along three transects in Trona (shown in Fig. 5). Transect TT1 was initiated at Mountain View Street, ultimately ending near the northeast corner of the Family Dollar store. Transect TT1 is approximately 325 m long with elevations (from Google Earth Pro, see Data and Resources) that range from 506 to 501 m AMSL (west to east), indicating an average ground-surface slope along the transect of approximately 1.6%. Figure 7 shows cumulative crack width versus distance along the transect. The sum of the ground crack widths measured along TT1 is 89 cm. Example images of ground cracks along Transect TT1 are shown in Figure 6h. We acknowledge that the sum of crack widths along a transect, as shown in Figure 7, may underestimate lateral movement, due to measurement errors or extensional features that do not manifest as cracks (Rathje, Dawson, *et al.*, 2017).

As shown in Figure 5, transect TT2 was oriented in a nearly north-to-south direction, starting near the northwest limit of

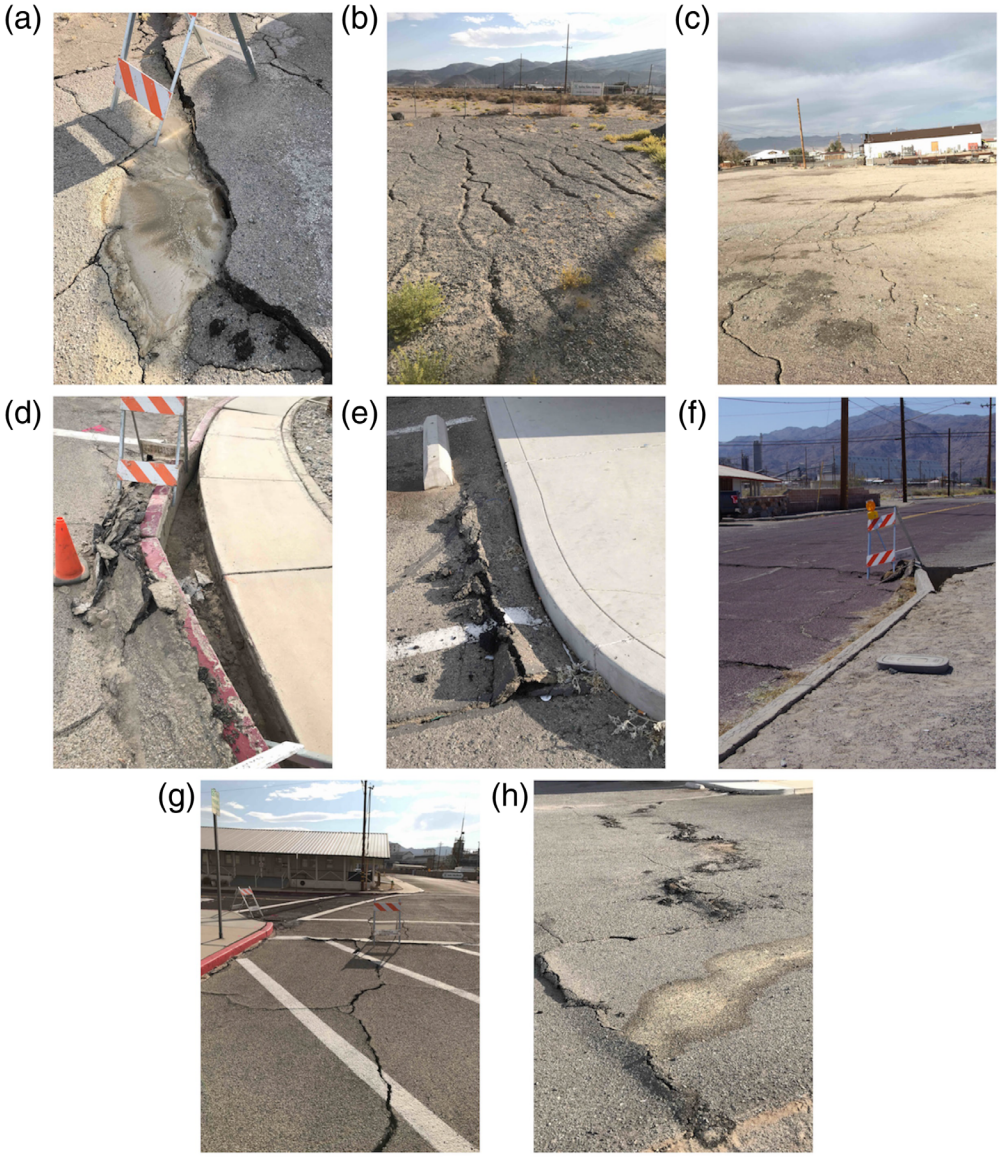

Figure 6. Ground failure from liquefaction in Trona. (a) Sand boil along a pavement crack created from lateral spreading (35.757483°, −117.37806°). (b,c) Extensional cracks caused by lateral spreading (35.757325°, −117.377705°; 35.75966°, −117.375892°). (d,f) Damaged asphalt from buckled curb edge (35.75936°, −117.37676°; 35.762387°, −117.372586°). (e,h) Compressional features from lateral spreading (35.75897°, −117.37561°; 35.75909°, −117.37552°). (g) Compressional and adjacent extensional features caused by lateral spreading and ground oscillation (35.75986°, −117.37651°). The color version of this figure is available only in the electronic edition.

the ground-failure region and ending at the Family Dollar parking lot. Transect TT2 is approximately 122 m long with elevations (from Google Earth Pro) that range from 503 – 500 m AMSL (north to south-southeast), indicating an average gradient of approximately 2.3%. As shown in Figure 7, the sum of the ground crack widths measured along TT2 is 71 cm. Example images of ground cracks along Transect TT2 are shown in Figure 6c.

Transect TT3 was initiated at the intersection of Magnolia Avenue and Argus Avenue and continued southeast, ending at the intersection of Argus Avenue and Trona Road. Transect TT3 is approximately 53 m long, and the elevation difference (from Google Earth Pro) is estimated as 2 m, indicating an average ground-surface slope along the transect of approximately 4%. The sum of the ground crack widths measured along TT3 is 45 cm. Example images of ground cracks along Transect TT3 are shown in Figure 6f.

The tension cracks in Trona that are documented in the transects occurred within a region that had been subject to pre-earthquake ground deformations. This was evident from patched cracks in pavement, some of which reopened during ground shaking. To the extent possible, the field teams sought to document "fresh" cracks that they believed opened during the earthquake, and only those features are included in the transects reported in Figure 7.

Liquefaction-related features were also observed in Argus (Fig. 8). The ground surface in the area shown as experiencing liquefaction has a gentle slope (~5%). The ground surface exhibited extensional cracks ranging from less than a millimeter to approximately 10 cm in width. The lateral spreading features became less frequent with proximity to the hills west of Argus and were more pervasive along the axis of a large alluvial fan (Fig. 3). A photographic survey was performed along a transect on A Street (designated transect AT1), approximately along the axis of the alluvial fan (Fig. 8). The transect was 457 m long with elevations (from USGS topographic map, see Data and Resources) that range from 499 to 524 m AMSL (from east to west), indicating an average ground-surface slope along the transect of approximately 5%. The extensional features were measured along Transect AT1 in Figure 8, with cumulative crack widths as shown in Figure 7. An example

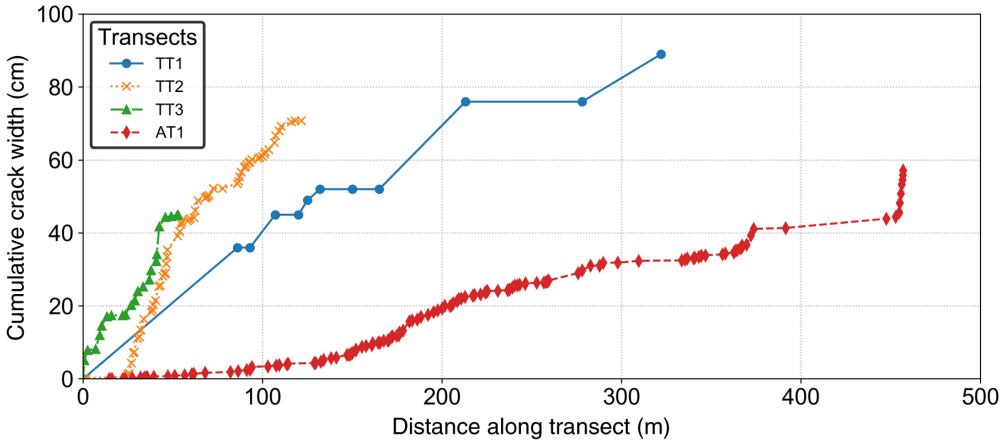

Figure 7. Cumulative crack width along transects in Trona and Argus. Transection locations are shown in Figures 5 and 8. The color version of this figure is available only in the electronic edition.

of lateral displacement cracking observed along Transect AT1 is shown in Figure S20. The sum of ground crack widths measured across the 457 m long transect was approximately 57 cm.

Whereas in Trona the documented lateral spread features were collocated with or nearby sand boils or other liquefaction surface manifestations, ejected material was not observed in Argus. Figure 8b shows transect AT1 along with the DPM produced following the earthquake sequence. At the intersection of A Street (AT1 transect) and Trona Road, nonzero damage proxies occur toward the southwest of the transect. At this location, the DPM helps identify the edges of this lateral spread feature.

A portion of the railroad track that passes through Argus was damaged, apparently by liquefaction-related ground movements, following the earthquake sequence. This feature occurred near the intersection of three different geologic units (gravel and sand, older alluvium, and sand and silt; Brandenberg, Stewart, *et al.*, 2020). Figure S21 shows photos taken on 6 July, although repair work was taking place. At this site, tension cracks and lateral spread openings were visible. An orthomosaic image, point cloud, and digital elevation model of the area (produced following completion of the repair works), showing the railroad repair zone, are available on DesignSafe (Winters *et al.*, 2019).

Ground-failure effects on buildings

Structures in the Towns of Trona and Argus appear to have been affected by liquefaction-induced ground failure and movement, primarily from lateral spreading. Figure 9 shows examples of buildings that experienced damage in Trona, some of which may have been liquefaction related. Figure 9a shows a 2.5 cm wide crack in the wall connecting the Esparza Restaurant and the adjacent building that occurred as a result of lateral spreading in combination with ground shaking. Figure 9b shows wall cracks on the eastern side of the Esparza Restaurant that has misaligned the door frame and caused the door to remain ajar. Figure 9c,d shows significant displacement and cracking of a sidewalk due to lateral spreading (there is a 0.5 L plastic bottle within the crack in Fig. 9c). Figure 9e,f shows structural damage in the form of large cracks in the floor slab of a museum due to lateral spreading, whereas Figure 9d shows a compressional crack in a sidewalk, along with damage to the adjacent building column. Figure 9h shows the Esparza Restaurant, which experienced wall cracks from lateral spreading in the **M** 6.5 event that were widened in the **M** 7.1 event, which the GEER team photographed after each event. It is possible that some of the observed cracks predated the earthquake sequence and were subsequently widened by the earthquake. The crack shown in Figure 9h on the eastern wall of the Esparza Restaurant building continued up to the roof, and the roof diaphragm was pulled apart, as shown in Figure 9i. Apparent effects of liquefaction on structures also occurred in Argus where structures that were heavily damaged were located on or near the alluvial fan, which exhibited evidence of lateral spreading in the form of tension cracks. Structural damage took the form of chimney separations from buildings, masonry cracks from extensional movements, toppled walls, and punch through in retention walls (Stewart *et al.*, 2019).

SEARLES LAKE

Searles Lake is a source of mineral-rich resources, which are mined by Searles Valley Minerals Inc. Main extraction activities at Searles Lake are based on solution mining operations involving wells that are used to extract brine. The brine is then processed to produce products such as salt, borax, boric acid, and sodium sulfate. Because a portion of the lake (mainly in the northwest area, next to Trona) is used continuously for mining activities, authorization is required to access the area. The first GEER team deployed in the region in July 2019 did not enter the mining zone.

Reconnaissance methods

As shown in Figure 1, the DPM produced following the Ridgecrest earthquake sequence indicates significant surface change within the Searles Lake area. High concentrations of nonzero SAR-based damage proxies are typically indicative of substantial damage and ground deformation. As a result,

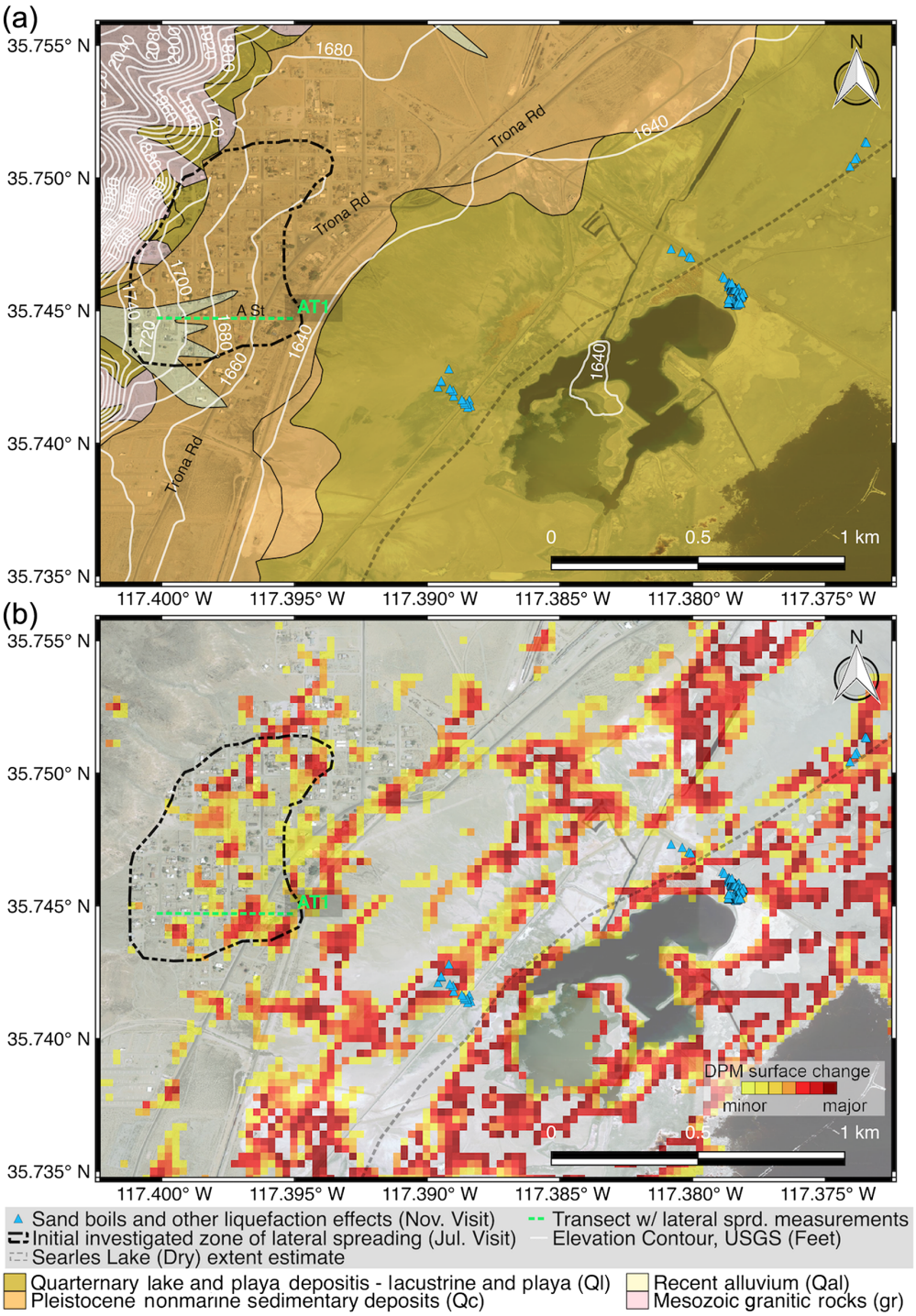

Figure 8. Map of Argus showing locations of observed liquefaction effects and lateral spreading measurement transects overlayed on (a) surface geology map and (b) DPM. Geologic units are labeled following descriptions from Smith (2009). Areas without indications of ground failure within investigated zone were inspected and hence are confirmed no ground-failure zones. The color version of this figure is available only in the electronic edition.

a second team requested and obtained authorization to access the area on 19 November 2019 to perform reconnaissance to evaluate potential ground deformations in the area. The areas of the lake visited during this reconnaissance mission are outside of the mining activity zones, and no extreme weather events occurred in the time between the earthquake mainshock and field deployment. As a result, we do not anticipate that the delay impacted our ability to document liquefaction features. Reconnaissance activities were performed with the assistance of Searles Valley Minerals personnel. This reconnaissance effort was performed utilizing geotagged photos, GPS track logs, and ground measurements. The results of this reconnaissance mission (maps and photographs) are available on DesignSafe (Zimmaro and Hudson, 2019).

Because the lake area is large (roughly 16×9 km), priority zones were selected using the DPM (Fig. S22). Nonzero damage proxies may be related to any surface changes. Because mining activities are concentrated in the northwest area of the lake, this zone may present surface changes from both earthquake-related ground failures and human activities. Our observations were made outside of the zones of mining activity (roughly located immediately south of Trona and north of 35.74°) and hence are likely to have resulted from earthquake-related ground failure.

The DPM in Figure 10 shows nonzero damage proxies roughly aligned with the lake margins. Portions of the lake boundary that exhibit such patterns include the northwest edge of the lake and two semicircular concentric zones in the southwest area of the lake. In the area of the lake southwest of Trona, a large portion of the lake is covered by a cluster of nonzero damage proxies, whereas in the area southwest of Argus, a large number of proxies are aligned along the lake margin. Figure 11 shows the USGS near real-time liquefaction hazard map produced following the **M** 7.1 mainshock. This map shows high

Figure 9. Ground failure effects on buildings in Trona. (a) Crack at screen wall between two buildings (35.75979°, −117.376315°). (b,h,i) Wall cracks at the eastern side of the Esparza Restaurant with associated sand ejecta and roof damage (35.75957°, −117.37611°). (c,d,g) Sidewalk pavement crack and offset likely from lateral spreading and ground oscillation (35.75982°, −117.37637°; 35.75978°, −117.37658°; 35.75980°, −117.37606°). (e,f) Cracks in floor slab from lateral spreading and ground oscillation (35.759802°, −117.376808°). The color version of this figure is available only in the electronic edition.

probability of liquefaction in the central zone of the lakebed. It predicts low or no liquefaction hazard along the lake margins.

Findings

Figure 10 shows the track log from the reconnaissance and locations of geotagged photos. Figure 10 also provides an overview of the reconnaissance findings. Figure 12a shows a photo of the central zone of the eastern edge of the lake (zone 1 in Fig. 10). This photo was taken from the road located southwest of the linear damage zone highlighted by the DPM. It shows a relatively narrow (about 110 m wide) zone covered by grayish ejecta with different coloration than surrounding material. This zone is potentially useful to study liquefaction susceptibility, as it is a clear example of variable liquefaction performance over a short length scale. At this location, the probability of

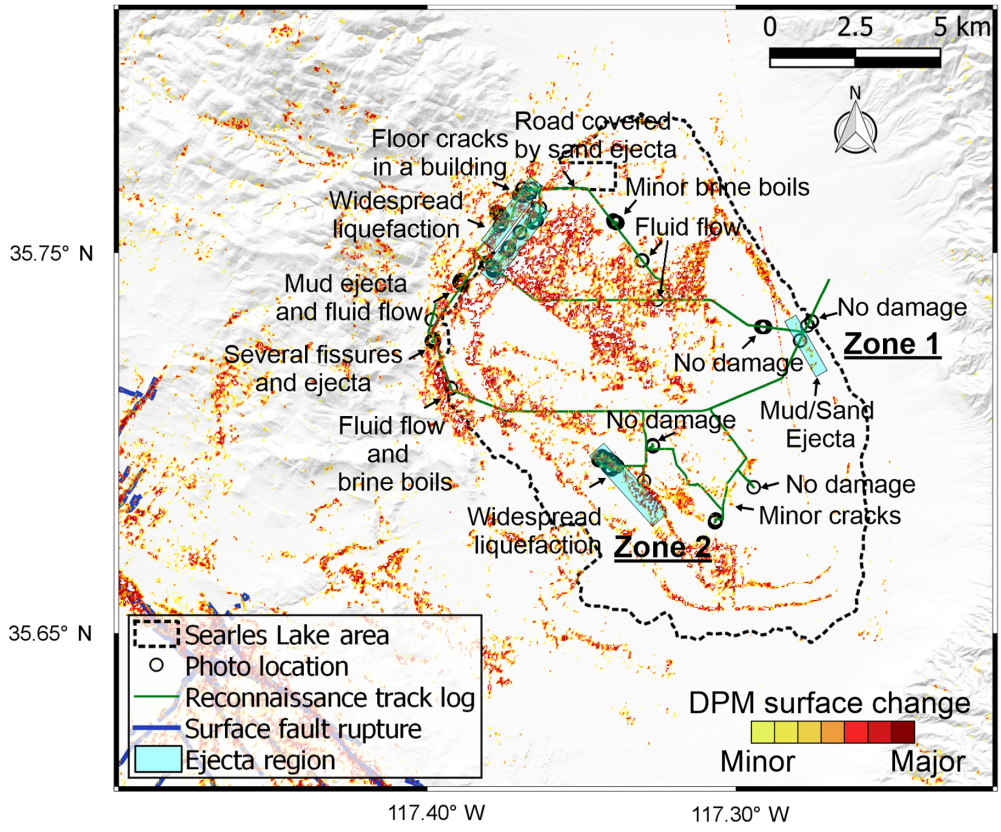

Figure 10. DPM produced following the **M** 7.1 event, route of the November 2019 reconnaissance mission, geotagged photo locations, and reconnaissance findings. The color version of this figure is available only in the electronic edition.

liquefaction predicted by the USGS liquefaction hazard map is ~4%.

Massive liquefaction was observed near the southwest edge of the lake (labeled zone 2 in Fig. 10). Thousands of sand boils (Fig. 12c), ground fissures and cracks (Fig. 12d), and abundant sand, gravel (Fig. 12d,e), and brine–evaporite ejecta (Fig. 12f), were observed along the relatively narrow northwest–southeast line depicted on the DPM. We use the term brine–evaporite to indicate that after the brine fluid was ejected onto the surface, evaporites precipitated out of the solution, as it evaporated. Figure 12f shows a sand boil entirely covered by a thin brine–evaporite layer. This sand boil covers an area containing sand from two smaller (and older) boils. Two hypotheses can be formulated to explain this phenomenon: (1) both manifestations occurred during the same event—the smaller sand boils were caused by liquefaction occurring in a more surficial layer, whereas the brine boil occurred in a deeper layer, or (2) the two liquefaction manifestations were triggered by separate events. The correct hypothesis cannot be identified from the available data, because reconnaissance was performed following the major events in the earthquake sequence. Within zone 2, the USGS liquefaction hazard map predicts a probability of liquefaction ranging between 5% and 8%.

Widespread liquefaction manifested in hundreds of sand boils, cracks, and fissures in the area southeast of Trona (highlighted in Fig. 10). Ground movements are also indicated in this area by the DPM. Similar observations were made on the northwest edge of the lake. In this broad north-northwestern zone of the lakebed, the USGS liquefaction hazard map predicts low (1%–2%) or zero probability of liquefaction.

Observations at Searles Lake confirmed ground deformation patterns reported in the DPM. Zones 1 and 2 in Figure 10 represent clear examples of DPM true positives (areas where nonzero damage proxies are present and ground-failure features are observed). True positives from the DPM were also observed in the area immediately southwest of Trona and at the southwest edge of the lakebed. Some spot checks were performed to identify potential true negatives (areas where colored damage proxies are not present and no ground deformations are observed). Such occurrences were observed in at least four zones in the south and southwest zones of the lakebed (labeled as "No damage" in Fig. 10). Neither DPM false positives (areas where nonzero damage proxies are present but no ground deformations are observed) nor DPM false negatives (areas where nonzero damage proxies are not present but ground deformations are observed) were observed at Searles Lake. However, these outcomes do not represent a comprehensive validation of the DPM at Searles Lake, as many areas were not accessed and inspected. Nonetheless, these preliminary findings are encouraging regarding the effectiveness of DPMs for the minimal-vegetation conditions in the Searles Lake area.

The USGS liquefaction hazard map predicts liquefaction in the lakebed region, but the actual observed deformation patterns are not consistent with the map. The mismatch is especially pronounced along the margin of the lakebed in which liquefaction was observed at various locations, but predicted liquefaction probabilities are low. False positives were also observed in the USGS liquefaction hazard maps. At two of the four locations labeled as "No damage" in Figure 11 (west of Zone 1), the USGS liquefaction hazard map predicted a

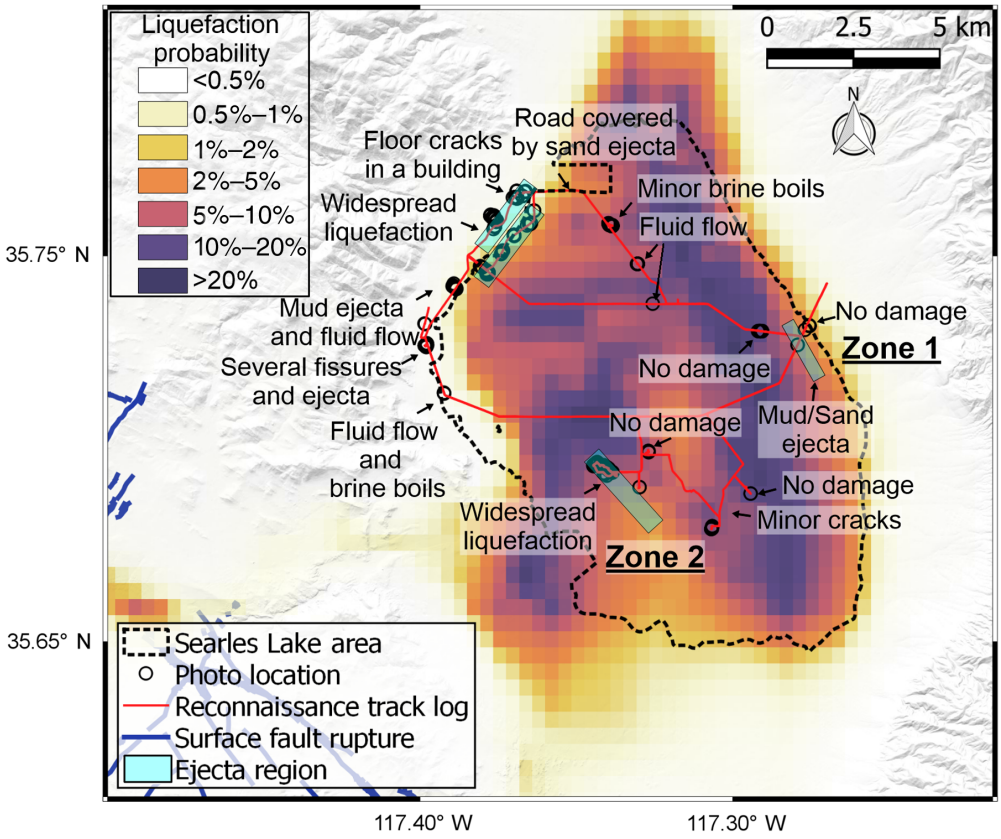

Figure 11. USGS liquefaction hazard map produced following the **M** 7.1 event, route of the November 2019 reconnaissance mission, geotagged photo locations, and reconnaissance findings. The color version of this figure is available only in the electronic edition.

relatively high probability of liquefaction of ~10%. This map correctly predicted a low (1%–3%) probability of liquefaction at a location east of zone 1, where no damage was observed.

In earlier sections of this article, we have presented many location-specific field observations and noted the degree of agreement with the DPM or USGS liquefaction hazard map. Here, we assemble the available findings. Doing so requires isolating potential liquefaction effects from other effects in the DPM—arguably this is not possible for the China Lake sites (due to proximity to surface rupture, which produces large movements that obscure liquefaction features) and human-occupied regions such as Trona and Argus (where anthropogenic effects add noise to the maps). This leaves the Searles Lake sites as providing the optimal conditions for the comparison.

We focus on the southern portion of the lakebed, south of 35.74°, where we have six sites in which liquefaction was observed and five sites without ground failure. For the purpose of the quantitative comparison, we use a 0.5% probability of liquefaction threshold for the USGS maps (i.e., ≥0.5% = liquefaction, <0.5% = no ground failure) and pixels with colorations for the DPM. Based on these thresholds, the "correct" predictions of field observations are made 10 of 11 times (~90%) for DPM and 5 of 11 times for the USGS map (~50%). Using a higher threshold probability of liquefaction, equal to 5%, the results are similar (correct predictions are made 5 of 11 times).

There are alternative means by which the utility of USGS maps can be assessed. Arguably, their purpose is not to identify specific locations of liquefaction and no-ground failure, but rather to highlight broader regions where liquefaction may or may not have occurred. Viewed from this perspective, region-wide quantitative metrics may be useful to assess performance. Again returning to the southern region of Searles Lake (surface area of 94.8 km^2), the percentage of land area identified by the DPM to have deformations is 18.7% (17.7 km^2), which given the favorable performance of the DPM to field observations can be taken as rough estimate of the percentage of land affected by liquefaction. The percentage of land area with probability of liquefaction greater than 5% and 10% from the USGS liquefaction hazard map is 57.3% (54.4 km^2) and 18.0% (17.1 km^2), respectively. These figures broadly agree with the field performance. Hence, although the USGS maps do not predict at a high percentage the specific locations of liquefaction, they do appear to correctly asses the percentage of affected land within the broader lakebed geomorphic province.

SUMMARY AND RESEARCH SIGNIFICANCE

We present liquefaction and related ground failures triggered by the 2019 Ridgecrest earthquake sequence. Observations presented in this article were collected as a result of a multiagency interdisciplinary collaboration among GEER, CGS, USGS, US Navy, and NASA. We present data on liquefaction manifestations including lateral spread features, sand boils, pavement cracks, fissures, and sand and gravel ejecta in three regions: (1) within NAWS China Lake, (2) in the towns of Trona and Argus located on the northeast margin of Searles Lake, and (3) within Searles Lake. Data collected in Trona, Argus, and the naval base were collected in July–August 2019 during the

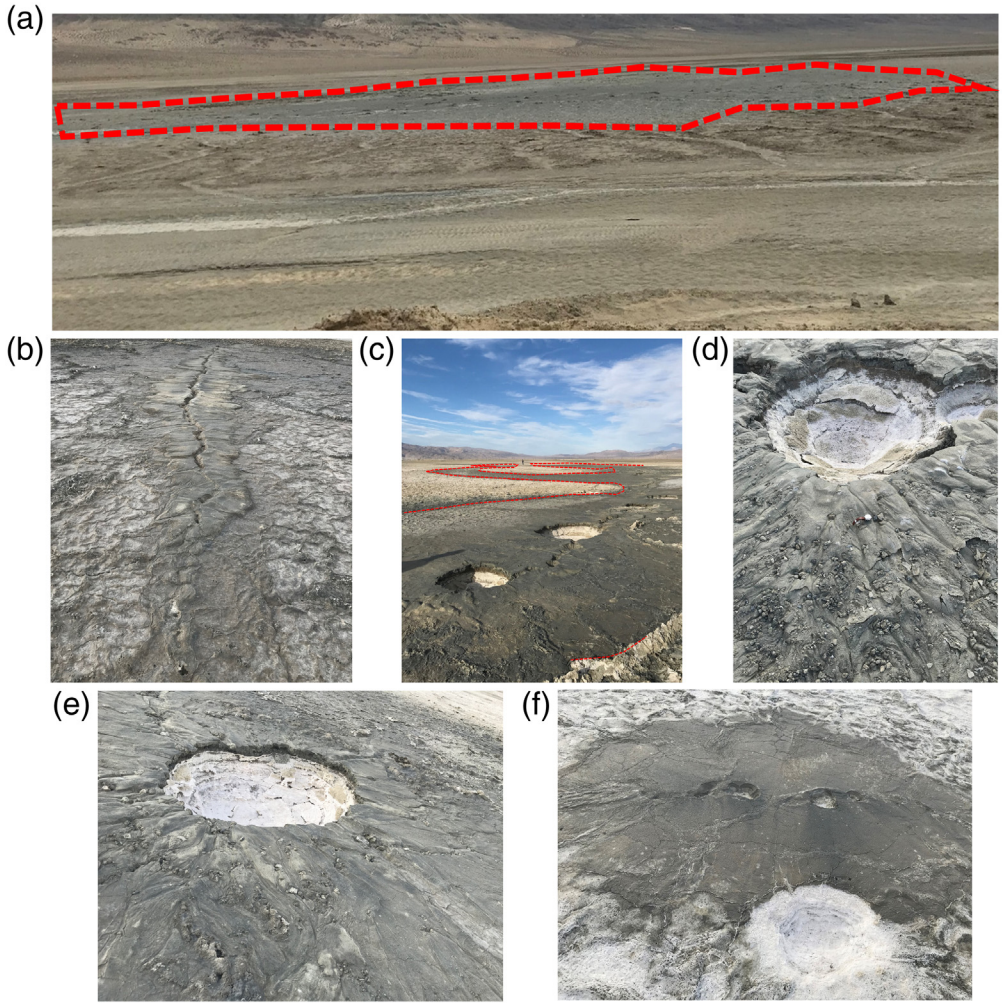

Figure 12. (a) Narrow liquefaction ejecta zone located in the central portion of the northeast edge of Searles Lake (35.72701°, −117.27801°). (b–f) fissures, sand boils with sand, gravel, and brine–evaporite ejecta observed toward the southwestern edge of the lake (35.694858°, −117.339622°; 35.6955°, −117.34235°; 35.695913°, −117.34113°; 35.695208°, −117.340462°; 35.695217°, −117.341072°). The color version of this figure is available only in the electronic edition.

GEER deployment, whereas data within Searles Lake were collected in November 2019. The latter deployment was organized using SAR-based DPMs as a guidance tool for planning and identification of priority areas.

The documentation of field performance presented in this article comprises one component of a liquefaction case history, with remaining components (not developed here) being ground-motion demands and geotechnical site conditions. With future work to develop those attributes, we anticipate that these case histories can impact future liquefaction models in the following respects:

- The well-documented lateral spread features in Trona and Argus along four transects can contribute to the development of lateral spread models for "ground slope" (not free-face) conditions.
- Variable ground performance with respect to the manifestation of liquefaction-induced ground failure over short length scales along former margins of Searles Lake could provide valuable insights into how subtle changes in soil composition or depositional environment affect liquefaction susceptibility.
- Ground-failure-related building damage in Trona and Argus may inform future models for effects of soil–structure interaction on building performance with liquefiable foundation soils.

Furthermore, the data presented in this article constitute a valuable resource for validating SAR-based DPMs and near real-time liquefaction hazard maps. The USGS liquefaction hazard maps are generated in near real-time following major earthquakes, whereas DPMs are produced within days following extreme events (including hurricanes, earthquakes, and wildfires). Both mapping approaches are still being calibrated and validated against observations. Thus, ground truth information is key for improving these products and their reliability. We find that the DPM identifies specific locations where surface change occurred. However, these maps cannot discern among different sources of deformation. The DPM performed particularly well in the southern portion of Searles Lake in which earthquake-induced surface changes were mostly related to liquefaction surface manifestations. More work is needed to quantitatively correlate raw coherence loss values with the percentage of land area covered by liquefaction surface manifestations (i.e., using high-resolution satellite imagery). The USGS liquefaction hazard map was not found to accurately identify specific liquefaction or no-ground failure locations, but was effective at identifying percentages of land with ground failure in an impacted geomorphic province (Searles Lakebed).

DATA AND RESOURCES

Seismic moments and resulting moment magnitudes were taken from the Global Centroid-Moment-Tensor (GCMT) project (Ekström *et al.*, 2012), available at https://www.globalcmt.org (last accessed June 2020). We prefer these magnitudes because they are well constrained from data derived from global seismic networks. The use of GCMT magnitudes conforms with Next Generation Attenuation procedures as described by Contreras *et al.* (2020). Fault traces from the Uniform California Earthquake Rupture Forecast, version 3 (UCERF3) model were retrieved from the California Geological Survey (CGS) open data portal at https://data.ca.gov/dataset/cgs-map-sheet-48-fault-based-seismic-sources-used-in-the-uniform-california-earthquake-rupture (last accessed May 2020). The damage proxy map used was retrieved from the National Aeronautics and Space Administration (NASA) Advanced Rapid Imaging and Analysis (ARIA) Jet Propulsion Laboratory (JPL) event page at https://aria-share.jpl.nasa.gov/20190704-0705-Searles_Valley_CA_EQs/DPM/ (last accessed January 2020). The USGS liquefaction hazard map produced following the **M** 7.1 mainshock was retrieved from the USGS event page at https://earthquake.usgs.gov/earthquakes/eventpage/ci38457511/ground-failure/summary (last accessed May 2020). The theoretical background of the USGS liquefaction hazard map used in this study is available at https://earthquake.usgs.gov/data/ground-failure/background.php (last accessed May 2020). The HydroSHEDS database is available at https://www.hydrosheds.org/ (last accessed June 2020). The distance from the coast dataset from the NASA Ocean Color Group is available at https://oceancolor.gsfc.nasa.gov/docs/distfromcoast/ (last accessed May 2020). Observation wells data were retrieved from the California Department of Water Resources (DWR) database at http://wdl.water.ca.gov/waterdatalibrary/groundwater/hydrographs/brr_hydro.cfm?CFGRIDKEY=23361 (last accessed May 2020). The USGS topographic map was retrieved from the USGS National Geospatial Program—US Topo at https://www.usgs.gov/core-science-systems/national-geospatial-program/us-topo-maps-america?qt-science_support_page_related_con=0# (last accessed May 2020). Elevation data were retrieved from Google Earth Pro (https://www.google.com/earth/versions/#earth-pro, last accessed May 2020). All maps were produced using QGIS (Open Source Geospatial Foundation Project, available at http://qgis.osgeo.org, last accessed January 2020). The unpublished manuscript by T. Dawson *et al.*, "Field-based observations of surface ruptures associated with the 2019 Ridgecrest earthquake sequence," submitted to *Bull. Seimol. Soc. Am.* A summary table of observations at the Naval Air Weapons Station (NAWS), China Lake, 19 figures showing liquefaction features at the at the NAWS, China Lake and Argus, and three maps are available in the supplemental material to this article.

ACKNOWLEDGMENTS

The Geotechnical Extreme Events Reconnaissance (GEER) association is supported by the National Science Foundation (NSF) through the Geotechnical Engineering Program under Grant Number CMMI- 1266418. Any opinions, findings, and conclusions or recommendations expressed in this material are those of the authors and do not necessarily reflect the views of the NSF. The GEER association is made possible by the vision and support of the NSF Geotechnical Engineering Program Directors Richard Fragaszy and the late Cliff Astill. GEER members also donate their time, talent, and resources to collect time-sensitive field observations of the effects of extreme events. Part of the research was sponsored by the NASA Earth Science Disasters Program (Grant Number 18-DISASTER18-0034) and performed in collaboration with the Jet Propulsion Laboratory and California Institute of Technology. Additional research support was provided by the Southern California Earthquake Center (SCEC), funded by the National Science Foundation (NSF) and U.S. Geological Survey (USGS), and by NSF RAPID Award Number EAR-1945781. We would like to thank Camille Anderson, Steven Kourakos, Adam Bingham, Dipti Barari, Devin Katzenstein at Searles Valley Minerals and Jade Zimmerman at Naval Air Weapons Station China Lake for assisting with the preparation and deployment of reconnaissance activities at Searles Lake in November 2019. We also thank Kate Allstadt, Eric Thompson, Alex Grant, Katherine J. Kendrick, Mike Diggles, Shane T. Detweiler, Timothy Dawson (Guest Editor) at USGS and one anonymous reviewer, whose constructive comments helped improving this paper. Any use of trade, firm, or product names is for descriptive purposes only and does not imply endorsement by the U.S. Government.

REFERENCES

Baise, L. G., and V. Rashidian (2017). Validation of a geospatial liquefaction model for noncoastal regions including Nepal, *Final Tech. Rept. for USGS Award G16AP00014*, Department of Civil and Environmental Engineering, Tufts University, Medford, Massachusetts.

Banks, E. W. (1982). Soil Liquefaction Potential at the Naval Weapons Center China Lake, California, *Master's Thesis*, University of Nevada, Reno, Reno, Nevada, NWC Technical Publication 6392, China Lake, California, 106 pp., 4 plates.

Berenbrock, C., and R. A. Schroeder (1994). The Ground-water flow and quality, and geochemical processes, in Indian Wells Valley, Kern, Inyo, and San Bernardino Counties, California, 1987–88, *U.S. Geol. Surv. Open-File Water-Res. Investig. Rept. 93-4003.*, Sacramento, California, 36 pp.

Brandenberg, S. J., C. A. Goulet, P. Wang, C. C. Nweke, C. A. Davis, M. B. Hudson, K. S. Hudson, S. K. Ahdi, and J. P. Stewart (2019). GEER field reconnaissance, in *Ridgecrest, CA earthquake sequence, July 4 and 5, 2019*, DesignSafe-CI, doi: 10.17603/ds2-vpmv-5b34.

Brandenberg, S. J., J. P. Stewart, P. Wang, C. C. Nweke, K. S. Hudson, C. A. Goulet, X. Meng, C. A. Davis, S. K. Ahdi, M. B. Hudson, *et al.* (2020). Ground deformation data from GEER investigations of Ridgecrest earthquake sequence, *Seismol. Res. Lett.* doi: 10.1785/0220190291.

Brandenberg, S. J., P. Zimmaro, J. P. Stewart, D. Y. Kwak, K. W. Franke, R. E. S. Moss, K. O. Cetin, G. Can, M. Ilgac, J. Stamatakos, *et al.* (2020). Next Generation Liquefaction database, *Earthq. Spectra* **36,** 939–959.

Bullard, T., S. Bacon, K. Adams, and D. Decker (2019). Geomorphic map of the China Lake basin below 700 m in support of Cultural Resource Management at Naval Air Weapons Station China Lake, Desert Research Institute for Naval Air Warfare Center Weapons Division, China Lake, California, NAWCWD Technical Publication 8839, available at https://apps.dtic.mil/dtic/tr/fulltext/u2/1077596.pdf (last accessed May 2020).

California Department of Water Resources (DWR) (2003). *California's Groundwater*, Bulletin 118, Update 2003, available

at https://cawaterlibrary.net/wp-content/uploads/2003/10/Bulletin_118_Update_2003.pdf (last accessed June 2020).

California DWR (2020). Water Data Library, available at http://wdl.water.ca.gov/waterdatalibrary/ (last accessed January 2020).

Contreras, V., J. P. Stewart, T. Kishida, R. B. Darragh, B. S.-J. Chiou, S. Mazzoni, N. Kuehn, S. K. Ahdi, K. Wooddell, R. R. Youngs, *et al.* (2020). Chapter 4: Source and path database, in data resources for NGA-subduction project, *PEER Rept. 2020/02*, J. P. Stewart (Editor), Pacific Earthquake Engineering Research Center, UC Berkeley (headquarters), Berkeley, California.

Ekström, G., M. Nettles, and A. M. Dziewonski (2012). The global CMT project 2004-2010: Centroid-moment tensors for 13,017 earthquakes, *Phys. Earth Planet. In.* **200/201,** 1–9.

Fan, Y., H. Li, and G. Miguez-Macho (2013). Global patterns of groundwater table depth, *Science* **339,** 940–943.

Field, E. H., R. J. Arrowsmith, G. P. Biasi, P. Bird, T. E. Dawson, K. R. Felzer, D. D. Jackson, K. M. Johnson, T. H. Jordan, C. Madden, *et al.* (2014). Uniform California earthquake rupture forecast, version 3 (UCERF3)—The time-independent model, *Bull. Seismol. Soc. Am.* **10,** 1122–1180.

Fielding, E. J., M. Talebian, P. A. Rosen, H. Nazari, A. Jackson, M. Ghorashi, and R. Walker (2005). Surface ruptures and building damage of the 2003 Bam, Iran, earthquake mapped by satellite Synthetic Aperture Radar interferometric correlation, *J. Geophys. Res.* **110,** no. B03302.

Franke, K. W., B. N. Lingwall, P. Zimmaro, R. E. Kayen, P. Tommasi, F. Chiabrando, and A. Santo (2018). A phased reconnaissance approach to documenting landslides following the 2016 Central Italy earthquakes, *Earthq. Spectra* **34,** 1693–1719.

Hijmans, R. J., S. E. Cameron, J. L. Parra, P. G. Jones, and A. Jarvis (2005). Very high resolution interpolated climate surfaces for global land areas, *Int. J. Climatol.* **25,** 1965–1978.

Ishitsuka, K., T. Tsuji, and T. Matsuoka (2012). Detection and mapping of soil liquefaction in the 2011 Tohoku earthquake using SAR interferometry, *Earth Planets Space* **64,** 22.

Jennings, O. P., J. L. Burnett, and B. W. Troxel (1962). Geologic Map of California–Trona Sheet, California Division of Mines and Geology (California Geological Survey), GAM 023, map scale 1:250,000, available at https://www.conservation.ca.gov/cgs/Documents/Publications/Geologic-Atlas-Maps/GAM_023_Trona/GAM_023_Map_1962.pdf (last accessed June 2020).

Jibson, R. W. (2020). Types and areal distribution of ground failure associated with the 2019 Ridgecrest, California, earthquake sequence, *Bull. Seismol. Soc. Am.*, doi: 10.1785/0120200001.

Jung, J., and S.-H. Yun (2020). Evaluation of coherent and incoherent landslide detection methods based on Synthetic Aperture Radar for rapid response: A case study for the 2018 Hokkaido landslides, *Remote Sens.* **12,** 265.

Kunkel, F., and G. H. Chase (1969). Geology and ground water in Indian Wells Valley, California, *U.S. Geol. Surv. Open-File Rept.*, 84 pp.

Lancaster, N., S. N. Bacon, T. F. Bullard, S. E. Baker, and D. L. Decker (2019). Eolian Hazard Assessment for the SNORT Facility, Desert Research Institute for Naval Air Warfare Center Weapons Division, China Lake, California, NAWCWD Technical Publication 8840, available at https://apps.dtic.mil/dtic/tr/fulltext/u2/1077597.pdf (last accessed May 2020).

McGraw, D., R. Carroll, G. Pohll, J. Chapman, S. Bacon, and R. Jasoni (2016). Groundwater resource sustainability: Modeling evaluation for the Naval Air Weapons Station, China Lake, Desert Research Institute for Naval Air Warfare Center Weapons Division, China Lake, California, NAWCWD Technical Publication 8811, available at https://apps.dtic.mil/dtic/tr/fulltext/u2/1070491.pdf (last accessed May 2020).

Ponti, D. J., J. L. Blair, C. M. Rosa, K. Thomas, A. J. Pickering, S. Akciz, S. Angster, J.-P. Avouac, J. Bachhuber, S. Bacon, *et al.* (2020). Documentation of surface fault rupture and ground deformation features produced by the Ridgecrest M 6.4 and M 7.1 earthquake sequence of July 4 and 5, 2019, *Seismol. Res. Lett.*, doi: 10.1785/0220190322.

Rathje, E. M., C. Dawson, J. E. Padgett, J.-P. Pinelli, D. Stanzione, A. Adair, P. Arduino, S. J. Brandenberg, T. Cockerill, M. Esteva, *et al.* (2017). DesignSafe: A new cyberinfrastructure for natural hazards engineering, *Nat. Hazards Rev.* **18,** 06017001.

Rathje, E. M., S. S. Secara, J. G. Martin, S. van Ballegooy, and J. Russell (2017). Liquefaction induced horizontal displacements from the Canterbury earthquake sequence in New Zealand measured from remote sensing techniques, *Earthq. Spectra* **33,** 1475–1494.

Schmitt, R. G., H. Tanyas, M. A. Nowicki Jessee, J. Zhu, K. M. Biegel, K. E. Allstadt, R. W. Jibson, E. M. Thompson, C. J. van Westen, H. P. Sato, *et al.* (2017). An open repository of earthquake-triggered ground-failure inventories (ver 2.0, December 2018), *U.S. Geol. Surv. Data Release*, doi: 10.5066/F7H70DB4.

Schweig, E. S., III (1984). Neogene tectonics and paleogeography of the southwestern Great Basin, Inyo County, California: Palo Alto, California, *Ph.D. Dissertation*, Stanford University, Stanford, California, 207 pp.

Sextos, A., R. De Risi, A. Pagliaroli, S. Foti, F. Passeri, E. Ausilio, R. Cairo, M. C. Capatti, F. Chiabrando, A. Chiaradonna, *et al.* (2018). Local patterns and incremental damage of buildings during the 2016 central Italy earthquake sequence, *Earthq. Spectra* **34,** 1639–1669.

Smith, G. I. (1979). Subsurface stratigraphy and geochemistry of late Quaternary evaporites, Searles Lake, California, *U.S. Geol. Surv. Profess. Pap. 1043*, 130 pp.

Smith, G. I. (2009). Late Cenozoic Geology and Lacustrine History of Searles Valley, Inyo and San Bernardino Counties, California, *U.S. Geol. Surv. Profess. Pap. 1727*, 115 pp., 4 plates.

Stewart, J. P. (Editor), S. J. Brandenberg, P. Wang, C. C. Nweke, K. S. Hudson, S. Mazzoni, Y. Bozorgnia, K. W. Hudnut, C. A. Davis, S. K. Ahdi, *et al.* (2019). Preliminary report on engineering and geological effects of the July 2019 Ridgecrest earthquake sequence, *Geotechnical Extreme Events Reconnaissance Association, Rept. GEER-064*, doi: 10.18118/G6H66K.

U. S. Geological Survey (USGS) (2020). Earthquake Catalog, available at https://earthquake.usgs.gov/earthquakes/search/ (last accessed April 2020).

Wald, D. J., and T. I. Allen (2007). Topographic Slope as a proxy for seismic site conditions and amplification, *Bull. Seismol. Soc. Am.* **97,** 1379–1395.

Wald, D. J., C. B. Worden, V. Quitoriano, and K. L. Pankow (2005). ShakeMap manual: Technical manual, user's guide, and software guide, *U.S. Geol. Surv., Techniques and Methods 12-A1*, available at http://pubs.usgs.gov/tm/2005/12A01/ (last accessed May 2020).

Warner, J. W. (1975). Ground-water quality in Indian Wells Valley, California, *U.S. Geol. Surv. Water-Res. Investig. Rept. 8-75*, 59 pp.

Winters, M. A., M.-P. C. Delisle, J. T. D. Lucey, Y. Kim, Z. Liu, K. S. Hudson, S. J. Brandenberg, and T. W. Gallien (2019). UCLA UAV imaging, in *Ridgecrest, CA Earthquake Sequence, July 4 and 5, 2019*, DesignSafe-CI, doi: 10.17603/ds2-wfgc-a575.

Worden, C. B., E. M. Thompson, M. Hearne, and D. J. Wald (2020). ShakeMap manual online: Technical manual, user's guide, and software guide, *U.S. Geol. Surv.*, doi: 10.5066/F7D21VPQ.

Yun, S., E. J. Fielding, M. Simons, P. Rosen, S. Owen, and F. Webb (2011). Damage proxy map of February 2011 M 6.3 Christchurch earthquake using InSAR coherence, *8th International Workshop on Advances in the Science and Applications of SAR Interferometry*, Frascati, Italy, 19–23 September 2011, available at https://earth.esa.int/documents/10174/1567329/Yun_FRINGE2011.pdf (last accessed January 2020).

Yun, S., K. Hudnut, S. Owen, F. Webb, M. Simons, P. Sacco, E. Gurrola, G. Manipon, C. Liang, E. J. Fielding, *et al.* (2015). Rapid damage mapping for the 2015 Mw 7.8 Gorkha earthquake using Synthetic Aperture Radar data from COSMO–SkyMed and ALOS-2 Satellites, *Seismol. Res. Lett.* **86,** 1549–1556.

Zhu, J., L. G. Baise, and E. M. Thompson (2017). An updated geospatial liquefaction model for global application, *Bull. Seismol. Soc. Am.* **107,** 1365–1385.

Zhu, J., D. Daley, L. G. Baise, E. M. Thompson, D. J. Wald, and K. L. Knudsen (2015). A geospatial liquefaction model for rapid response and loss estimation, *Earthq. Spectra* **31,** 1813–1837.

Zimmaro, P., and K. Hudson (2019). Searles lake liquefaction, in *Ridgecrest, CA earthquake sequence, July 4 and 5, 2019*, DesignSafe-CI, doi: 10.17603/ds2-9wp5-rp81.

Manuscript received 17 January 2020
Published online 21 July 2020